metals

Article

Resistance Spot-Welding of Dissimilar Metals, Medium Manganese TRIP Steel and DP590

Fufa Wei [1,2], Yunming Zhu [1,2], Yifeng Tian [1,2], Hongning Liu [1,2], Yongqiang Zhou [1,2] and Zhengqiang Zhu [1,2,*]

[1] Advanced Manufacturing School, Nanchang University, Nanchang 330047, China
[2] Jiangxi Provincial Key Laboratory of Robot and Welding Automation, Nanchang 330000, China
* Correspondence: zhuzhq01@126.com

Abstract: Resistance spot-welding of dissimilar metals, medium manganese TRIP steel 7Mn and DP590, is carried out. The effects of single-pulse welding parameters and a double-pulse-tempering current on the quality characteristic parameters and mechanical properties of 7Mn/DP590 spot-welded joints are studied. The welding process parameters are optimized using the control variable method. The results show that the optimal process parameters under a single pulse are as follows: electrode pressure: 4.5 kN, welding current: 9 kA and welding time: 300 ms. The failure mode of the welding joint is partial pull-out failure (PF-TT). The welding parameters have great influence on the nugget diameter and thickness reduction. Expulsion, crack and shrinkage are displayed in the joint under high electrode pressure. Softening occurs in the heat-affected zone due to a strong halo effect in the single-pulse weld. The tempering zone on the DP590 side is 202.49 HV, which is the lowest hardness point, while the hardness of the nugget zone is 450 HV. The addition of the tempering current homogenizes the microstructure with different failure paths and eliminates the stress. The tensile shear force of the joint increases by 17.13%. The 7Mn Steel/DP590 resistance spot-welding joint is from the fusion line to the center of the nugget, and the microstructure is composed of plane crystal, cellular crystal, dendritic crystal and columnar crystal, in turn. The nugget zone is composed of lath martensite and a small amount of residual austenite. Fine quasi-spherical and lamellar interbedded cementites are formed in the tempering zone of the DP590-side heat-affected zone.

Keywords: resistance spot-welding; medium manganese TRIP steel; microstructure; mechanical properties; DP590

check for updates

Citation: Wei, F.; Zhu, Y.; Tian, Y.; Liu, H.; Zhou, Y.; Zhu, Z. Resistance Spot-Welding of Dissimilar Metals, Medium Manganese TRIP Steel and DP590. *Metals* **2022**, *12*, 1596. https://doi.org/10.3390/met12101596

Academic Editor: Sergey Konovalov

Received: 22 August 2022
Accepted: 19 September 2022
Published: 25 September 2022

1. Introduction

With the increasing demand for lightweight automobiles, the application of advanced high-strength steel in the automobile industry is expanding because it can meet the requirement of light weight and take into account the safety performance of the automobile. It is known that for every 1% reduction in vehicle mass, the fuel efficiency can be increased by 0.6–0.8%, and the CO2 emissions can be reduced by 0.45% [1–5]. Therefore, the realization of a lightweight body has become the key to automobile R & D and to helping manufacturing and automobile enterprises to improve their competitiveness. As the third generation of advanced high-strength steel, the microstructure of medium manganese TRIP steel (7Mn Steel) is mainly composed of martensite, ferrite and retained austenite, and makes full use of low-cost alloying elements (mainly C, Mn, Al, Si, etc.) to enhance strength and plasticity. Its excellent performance can easily meet the requirements of light weight and safety in automobiles, and it has become the focus of research in recent years. The retained austenite is mainly via critical annealing and inverse transformation annealing, and the comprehensive mechanical properties of the steel are improved by using the TRIP effect of austenite [6–11]. DP steel is a multiphase steel composed of reinforced-phase martensite, bainite or austenite and matrix ferrite [12]. Due to its energy absorption effect in automobile collisions, it improves the safety of automobiles and is widely used in the automobile industry [13]. The promotion and application of medium manganese steel in the automobile industry is inseparable from advanced connection technology with high quality and high efficiency. Resistance spot-welding has become one of the main connection technologies in automobile manufacturing due to its advantages of high production efficiency, low cost, the easy guarantee of welding quality and the easy realization of automation. The welding of sheets and medium-thick sheet parts in the automobile body structure is usually completed using resistance spot-welding, accounting for about 90% of the total assembly workload of the body [14–16]. Therefore, the strength of a resistance spot-welding joint of medium manganese steel and the stability of the process are crucial to the comprehensive performance and safety and stability of the vehicle, respectively. However, the hardening tendency of these two steels is large, and the welded joints are prone to high internal stress and low plasticity, which seriously reduces the joint performance. Therefore, in this paper, double-pulse welding is used to reduce the residual stress and improve the mechanical properties of the joint. The theoretical effect is that the first welding pulse will make the weld nugget fully hardened. Using a reasonable tempering pulse, heat treatment can be carried out using a tempering current, which can effectively reduce the influence of residual stress on joint quality, improve joint structure and optimize the joint failure mode and mechanical properties [17].

At present, most of the studies on the heat treatment of the third generation of medium manganese TRIP steel for automobiles are conducted in China and abroad, while there are few studies on resistance spot-welding of dissimilar metals such as medium manganese TRIP steel and other steels. For example, Qiang Jia [18] from Tsinghua University conducted resistance spot-welding on cold-rolled 5Mn medium manganese steel. The results show that the retained austenite mainly exists in the heat-affected zone and its content decreases with the increase in the distance from the base metal. Gitae Park [19] conducted resistance spot-welding on medium manganese TRIP steel (MT/MT) and medium manganese steel and DP980 dissimilar steel (MT/DP), respectively. It was found that the MT/MT welding spot and the MT/DP welding spot have different weld failure modes. The increased brittleness in the coarse-grain zone of MT steel was due to the decrease in residual austenite content and the insufficient self-tempering effect of martensite. Then, Gitae Park [20] conducted a tempering study. It was found that tempering heat treatment can improve the tensile strength (CTS) of MT/DP welding spots. After tempering heat treatment, the failure mode of the welding spots changed from pull-out failure to partial pull-out failure. The resistance spot-welding of medium manganese steel was studied by Li [21]. It was found that adding gaskets between workpieces can significantly improve the peak load, energy absorption rate and elongation of welded joints. The failure mode of the welding spot changed from interfacial fracture (IF) to PF. Sun et al. [22] studied the effect of the Si element on the deformation mechanism of medium manganese steel. The change in solid-solution Si content will affected the strain distribution between ferrite and austenite and the different degrees of twin deformation in austenite, thus increasing the strain hardening rate and uniform elongation. Chun Quan Liu et al. [23] studied medium manganese (TRIP) steel under hot-rolling and cold-rolling conditions. Both hot-rolled and cold-rolled experimental steels show excellent mechanical properties after quenching and tempering (Q & T) heat treatment. The mechanical properties of cold-rolled quenched and tempered steel after isothermal treatment at 775 °C for 1 h were better than those of hot-rolled quenched and tempered steel due to the TRIP effect produced by a large amount of retained austenite. Lun et al. [24] studied the fiber laser-welding of medium manganese TRIP steel with different combinations of high-strength low-alloy (HSLA) and dual-phase (DP980) steels. The fusion zone (FZ) of the joint was mainly composed of martensite and some interdendritic austenite, which was stabilized by more manganese, and the FZ of different combinations with HSLA and DP980 steel was mainly composed of martensite. Under uniaxial tension, the failure of the medium manganese TRIP laser-weld occurred near the local strain-accumulated FZ.

In this study, resistance spot-welding of third-generation high-strength steel medium manganese TRIP steel and DP590 dissimilar steel was carried out through a double-pulse resistance spot-welding process. The mechanical properties, fracture mode and mechanism were studied to solve the connection problem of lightweight materials. This has important theoretical significance and engineering application value for the application of medium manganese TRIP steel/DP590 dissimilar advanced high-strength steel.

2. Materials and Method

In this paper, double-pulse resistance spot-welding experiments on 1.6 mm-thick medium manganese steel and 1.2 mm-thick DP590 dual-phase steel, produced by Baosteel(shanghai, China), were carried out using the X-type medium-frequency DC spot-welding machine RSW-2 produced by the SUNKE company(Tianjin, China). Figure 1 shows the microstructure images of medium manganese TRIP steel (hereinafter referred to as 7Mn Steel) and the DP590 base metal. As shown in Figure 1a,b, the DP590 base metal is a dual-phase structure of ferrite(F) and martensite(M), and the reinforcement is distributed in an island-like manner on the ferrite matrix. As shown in Figure 1c,d, the parent material of 7Mn Steel is the dual-phase structure of ultrafine-grained ferrite and ultrafine-grained retained austenite(RA), in which the retained austenite has two kinds of spherical and lamellar austenite. The chemical compositions and mechanical properties of 7Mn Steel and DP590 are shown in Tables 1 and 2, and a schematic diagram of the welded joints is shown in Figure 2. The types of elements in DP590 and 7Mn TRIP steel are complex. According to the formula of carbon equivalents (1), the carbon equivalents of DP590 and 7Mn Steel are 1.31% and 0.38% [25].

$$C_{eq} = (C + \frac{Mn}{6} + \frac{Cr + Mo + V}{5} + \frac{Ni + Cu}{15}) \times 100\%. \quad (1)$$

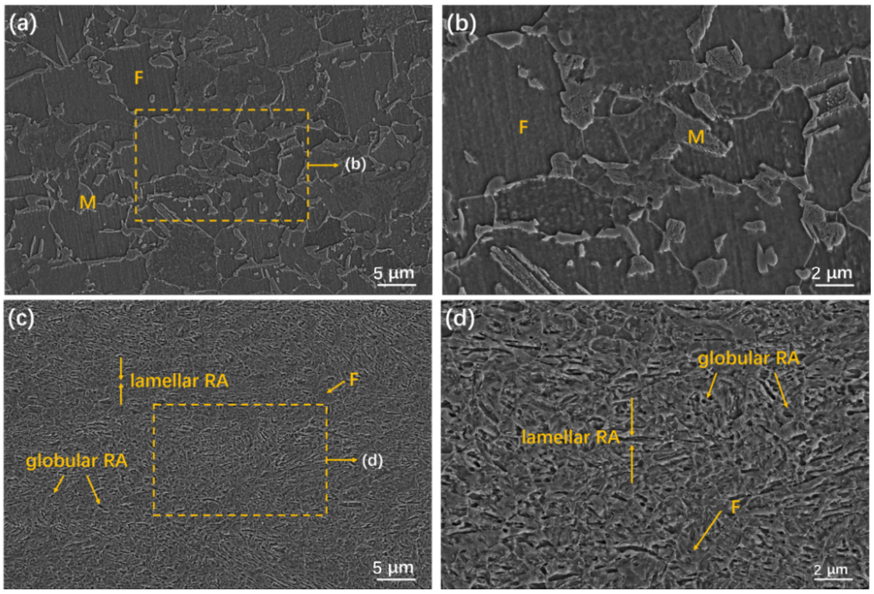

Figure 1. Microstructure of 7Mn Steel BM and DP590 BM: (**a**,**b**) DP590 BM; (**c**,**d**) 7Mn Steel BM.

Table 1. Chemical composition of 7Mn Steel and DP590.

Base Metal	C	Mn	Si	Cr	Al	N	Pb	P	S
DP590	0.071	1.84	0.43	-	-	-	-	0.011	0.02
7Mn	0.13	6.98	0.22	0.09	0.04	0.0099	0.008	0.006	0.0011

Table 2. Mechanical properties of 7Mn Steel and DP590.

Base Metal	Yield Strength (MPa)	Tensile Strength (MPa)	Elongation (Pct)
7Mn Steel	1580	1664	16.5
DP590	488	737	32.3

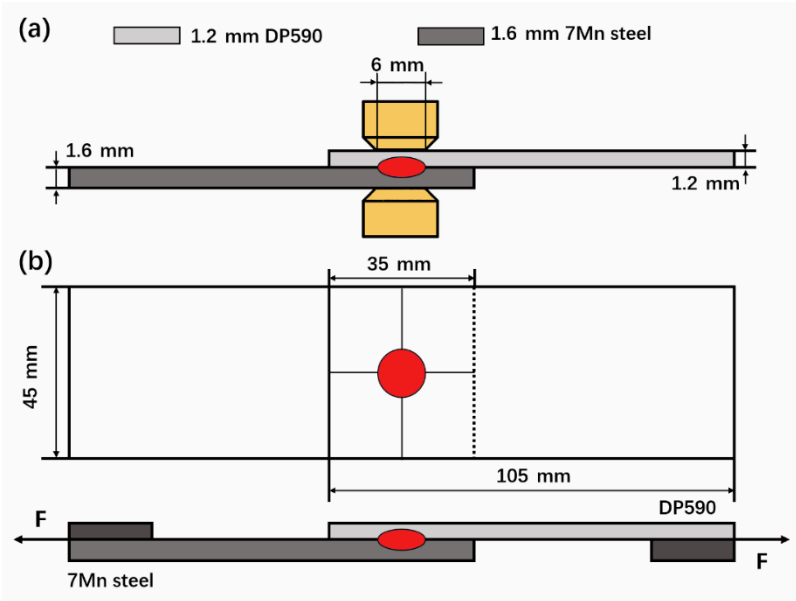

Figure 2. Mechanical test specimen: (**a**) lap type; (**b**) tensile specimen size.

The effects of welding current, welding time and electrode pressure on the quality characteristic parameters of welding spots and the mechanical properties of joints were studied by means of SEM and a microhardness tester using the control variable method, as shown in Figure 3a. The optimal process parameters under a single pulse were determined, that is, the nugget diameter was the largest, the mechanical properties were the best and the failure mode tended toward PF without expulsion. On the basis of single-pulse optimum process parameters, the tempering current was added, and the tempering current and cooling time were changed to explore the improvement effect of tempering current on the quality of resistance spot-welding of medium manganese TRIP steel/DP590 dissimilar steel, as shown in Figure 3b. The tensile shear specimens were tested using a universal testing machine (INSTRON5982, Instron, Norwood, MA, USA) at a tensile speed of 1 mm/min. The microstructure of the weld was analyzed using a super-depth-of-field metallographic microscope (VHX-6000, Keynes, Osaka, Japan) and a scanning electron microscope (Merlin Compact, Zeiss, Stuttgart, Germany). The micro-Vickers hardness tester was used to measure the hardness under a load of 500gf.

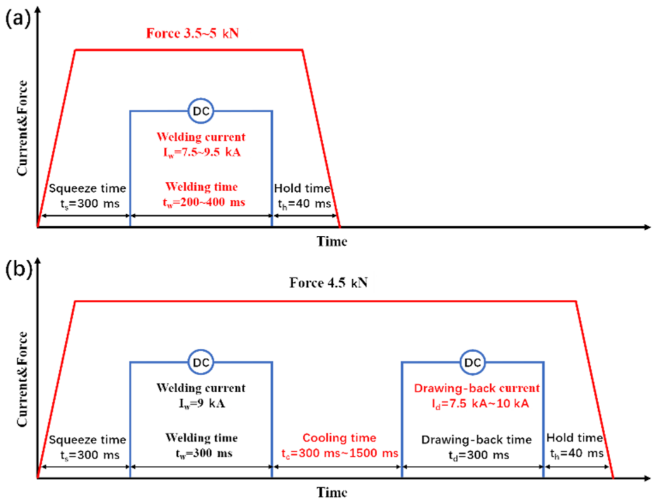

Figure 3. Welding process diagram: (**a**) single pulse; (**b**) tempering current.

3. Results and Discussion

3.1. Influence of Single-Pulse Welding Process

When the welding time is 300 ms and the electrode pressure is 4.5 kN, the welding current increases gradually from 7.5 kA to 9.5 kA every 0.5 kA. As shown in Figure 4a,d, it can be seen from the figure that the thickness reduction is positively correlated with the size of the welding current. The thickness reduction increases with the increase in the welding current, and the nugget diameter first increases, and then, decreases with the increase in the welding current. When the welding current is 9 kA, the maximum value is 8.53 mm. This is due to the increase in the welding heat input caused by the increase in the welding current. The more the amount of metal melted in the nugget increases, the more fully the nugget is formed, and the larger the nugget diameter. However, when the current reaches 9.5 kA, the growth rate of the nugget is too fast to exceed that of the plastic ring. The molten liquid cannot be cooled, and the liquid is sprayed out from the nugget under the action of pressure, resulting in expulsion. Expulsion takes away part of the liquid metal with high heat. There is not enough metal to form the nugget, and the nugget of the welding spot becomes smaller. The tensile shear force of the joint increases first to 11.44 kN, and then, stabilizes with the increase in current. The failure mode of the welding spot is PF-TT failure when the welding current is 9 kA, and the specimens are all IF. It can be seen from the figure that the thickness reduction is positively correlated with the size of the welding current, and the thickness reduction increases with the increase in the welding current. At the same time, it can be found that the thickness reduction of the 7Mn Steel side is always greater than that of the DP590 side, which may be related to the TRIP effect of 7Mn Steel. Due to the existence of the TRIP effect, the plasticity of 7Mn Steel is improved, and more deformation occurs under stress compared with DP590, resulting in the transformation of residual austenite to martensite. Pouranvari et al. [26] found that expulsion did not reduce the carrying capacity of the joint, but could reduce its energy absorption capacity. When the welding current is 9.5 kA, the welding spot takes away part of the metal due to internal expulsion (between the two workpieces), resulting in a relatively large thickness reduction and deterioration of the joint. So, when the welding current is 9.5 kA, the tensile shear force of the spot-welded joint does not decrease significantly, but the failure mode of the welding spot is transformed into IF failure.

At a fixed welding current of 8.5 kA and electrode pressure of 4.5 kN, the welding time gradually increases from 200 ms to 400 ms every 50 ms. The results are shown in Figure 4b,e. The nugget diameter increases with the increase in the welding time, and reaches a maximum value of 8.45 mm at a welding time of 400 ms. There is no expulsion phenomenon. At this time, the failure mode of the welding spot is PIF failure, and the specimens are IF failure. The thickness reduction increases with the increase in welding time, and the reason is the same as that of the influence of welding current on the thickness reduction. When the welding time is 400 ms, the thickness reduction of the DP590 side is 15.46%, and the thickness reduction of the 7Mn Steel side is 16.53%, which does not exceed 20% of the welding specification, both of which are qualified as thickness reductions. Comparing Figure 4a,b, it can be seen that the influence of welding spot time on nugget diameter and thickness reduction is less than that of welding current, which can be explained from the total heat production of the nugget according to Joule's law. The current affects heat production in the form of a square, so the influence is higher. With the increase in welding time, the change in the tensile shear force of the spot-welding joint is not obvious. When the welding time is 200 ms, the tensile shear force is 10.79 kN, and when the welding time is 400 ms, the tensile shear force is 11.22 kN; there is little difference. However, the failure mode of the joint changes from IF failure to PIF failure. It is explained that due to the increase in welding time, the internal metallurgical reaction of the nugget is more sufficient, the nugget size is increased, the joint strength is improved and the electrode indentation is increased [16]. The welding current density is reduced, the heat production efficiency is decreased and the heat dissipation efficiency is increased, which offsets part of the heat production, so the mechanical properties of the joint are slowly improved [27].

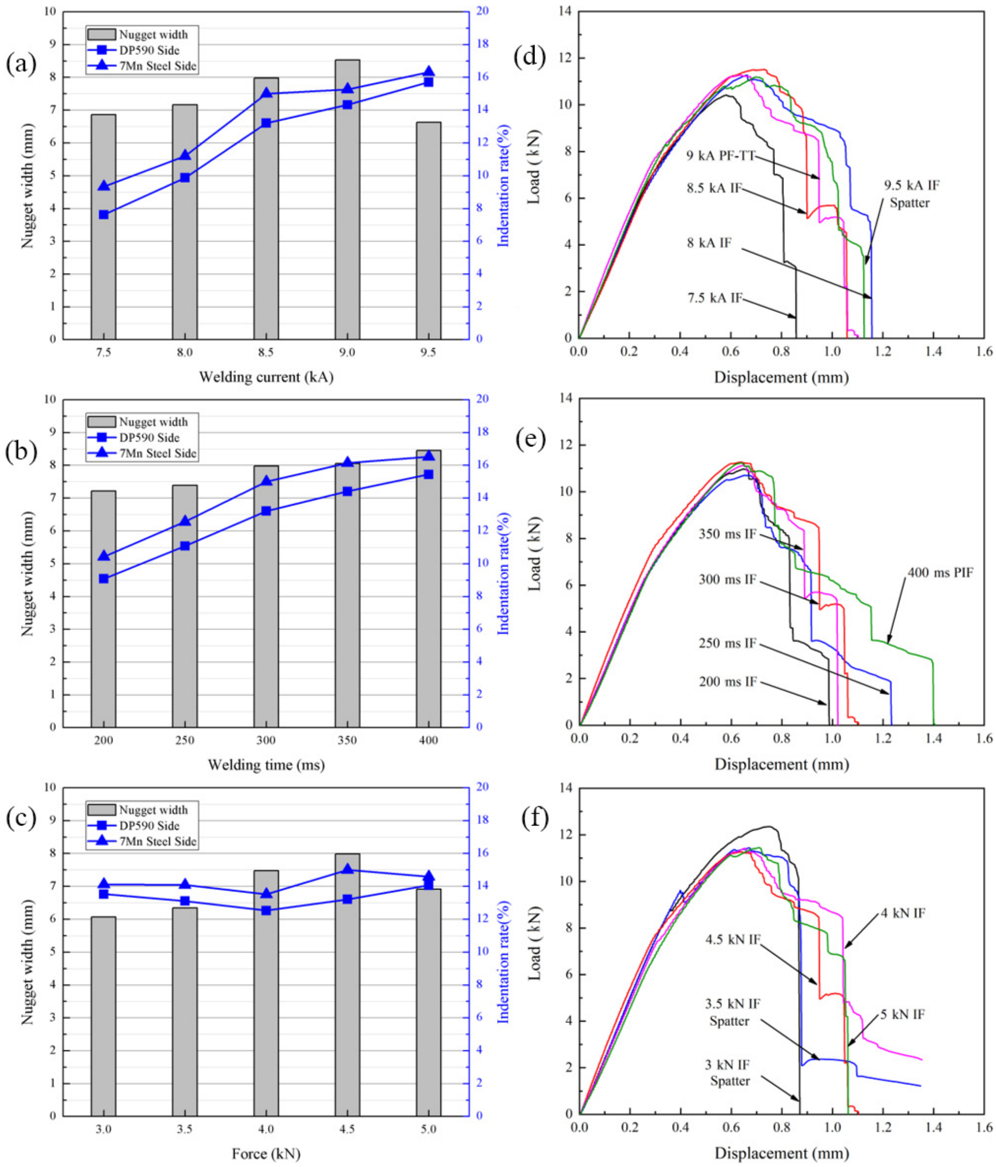

Figure 4. (**a**–**c**) Influence of different process parameters on characteristic parameters of joint quality; (**d**–**f**) load–displacement curves under different process parameters.

When the welding current is 8.5 kA and the welding time is 300 ms, the electrode pressure increases gradually from 3 kN to 5 kN every 0.5 kN. The results are shown in Figure 4c,f. The nugget size first increases, and then, decreases with the increase in electrode pressure. Too small electrode pressure at the beginning of welding results in too small contact area between workpieces and between electrodes and workpieces and increased contact resistance, thus, the current density, total resistance and heating speed are too large, resulting in expulsion, resulting in the nugget diameter of the welding spot being too small. When the electrode pressure is 3 kN and 3.5 kN, the nugget diameter is only 6.07 mm and 6.35 mm, respectively. When the electrode pressure is 4.5 kN, the nugget diameter is 7.99 mm. When the electrode pressure reaches 5 kN, the contact area of the three pairs of contact surfaces is too large, and the heat generated for nucleation is insufficient. Finally, the nugget diameter of the welding spot is reduced to 6.915 mm, and the excessive electrode force causes the plastic ring to be crushed to produce cracks and an expulsion phenomenon, as shown in Figure 5a. Finally, the shrinkage cavity defect is generated in the nugget center, as shown in Figure 5b. With the increase in electrode pressure, the tensile shear force of the spot-welding joint remains stable without obvious change. The failure mode of welding spots is IF failure. The thickness reduction of the welding spots does not change significantly with the electrode pressure.

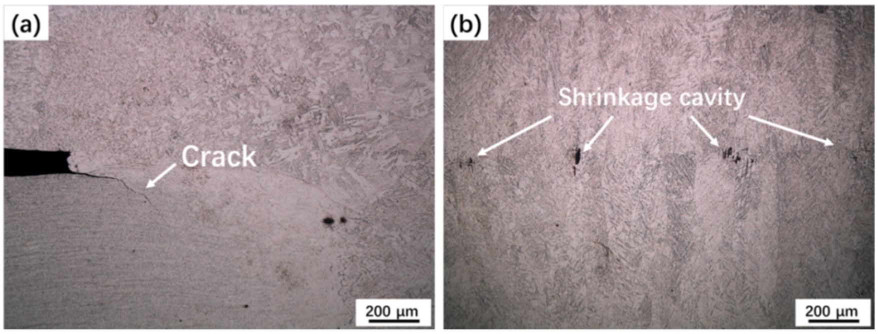

Figure 5. Welding defects of joint under 5 kN electrode force: (**a**) crack; (**b**) shrinkage cavity.

3.2. Influence of Double-Pulse-Tempering Process

The tempering current was added under the optimum process parameters of a single pulse; when the cooling time is fixed at 1500 ms, the tempering current gradually increases from 7.5 kA to 9.5 kA with each 0.5 kA interval, as shown in Figure 6a. With the increase in tempering current, the nugget size increases slightly, and the tensile shear force reaches the maximum value (12.96 kN) at a tempering current of 7.5 kA. This is because the tempering current causes more materials to participate in the metallurgical reaction, which increases the nugget size and improves the peak load. However, when the stress is eliminated, the larger tempering current causes coarsening of the microstructure. With the increase in tempering current, the coarsening of the microstructure is dominant, and the tensile shear force of the joint decreases. At a constant tempering current of 8.5 kA, the cooling time increases from 300 ms to 1800 ms every 300 ms. As shown in Figure 6b, the nugget size increases slightly with the increase in cooling time, and the tensile shear force does not change much. The reason is similar to the effect of the tempering current. Compared with a larger cooling time, the microstructure after a smaller cooling time is thicker. It is also found that the addition of the tempering current does not change the failure mode of the welding spots, and all the welding spots are PF-TT failure.

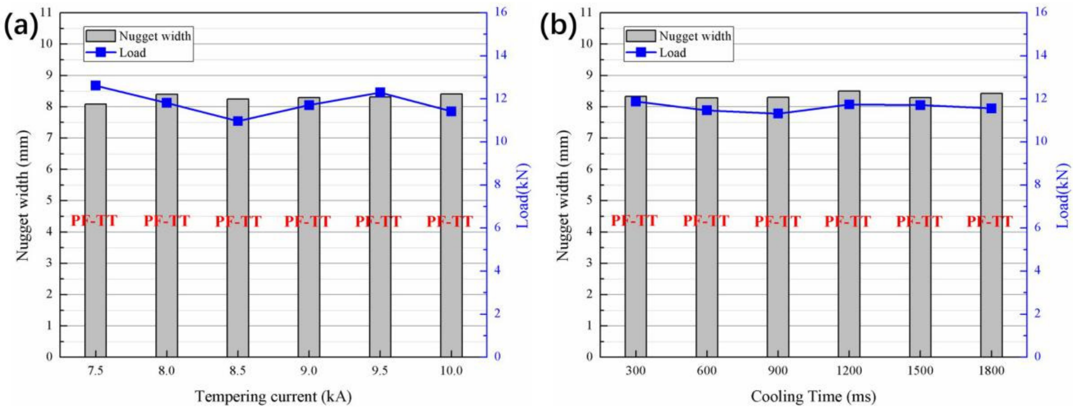

Figure 6. Welding data when adding tempering current: (**a**) change in tempering current; (**b**) change in cooling time.

The microhardness distribution obtained under the optimal single-pulse welding process and after adding the pulse-tempering current is shown in Figure 7a,b. The tempering current is 7.5 kA and the cooling time is 1500 ms. The hardness of the nugget part is stable at about 450 HV. It can be seen that the untempered joints have different degrees of softening zone in the heat-affected zone. The hardness of the nugget zone has no obvious change compared with that under the single-pulse condition, indicating that the nugget formed under the initial pulse current completely melted again under the second pulse current. After the addition of the tempering current, the softening zone and two obvious tempering lines are displayed in the heat-affected zone of the DP590 side. The hardness of SC1 and SC2 is 205.43 HV and 258.03 HV, respectively. In previous studies the phenomenon of failure around the fusion zone in relation to the instantaneous softening of the fusion boundary was called a halo [28], and this decrease in hardness provides evidence of halos in these welds. The existence of this softening zone may be the cause of failure around the fusion zone. Figure 7c shows the tensile shear-displacement curve of the spot-welding joint before and after tempering. It can be seen from the figure that after adding the tempering current with a cooling time of 1500 ms and tempering current of 7.5 kA, the tensile shear force increases from 11.44 kN to 13.4 kN. Although the failure mode of the welding joint is not changed, the tensile shear force increases by 17.13%, and the displacement distance is improved to some extent. This is because the tempering pulse eliminates part of the residual stress, which improves the quality of the joint, especially the heat-affected zone on the 7Mn Steel side.

Figure 8 shows the optimal process: When the welding current I = 9 kA, the welding time T = 300 ms, the electrode pressure F = 4.5 kN, the pulse-tempering current is added, the tempering current is 7.5 kA and the cooling time is 1500 ms; the welding parameters measured by the welding monitoring system are obtained. The dynamic resistance curve decreases rapidly at the beginning of welding, and then, slowly decreases to be stable after a slight rise. With the progress of welding, the resistivity of DP590 and 7Mn Steel increases with the increase in temperature. At the same time, when the temperature is higher than the austenite transformation temperature (727 °C), the martensite and ferrite in the material are transformed into austenite, which further increases the internal resistance of the workpiece [27], resulting in a rise in the dynamic resistance curve. When the weld nugget begins to melt into liquid metal, since the electron moves in the liquid phase more easily than in the solid phase, with the rapid growth of the weld nugget and the increase in the liquid phase, the influence of phase transformation on the resistivity dominates in a very short time, and the dynamic resistance curve decreases rapidly. When the nugget diameter reaches the maximum value, the resistance heat decreases with the decrease in the dynamic resistance, and the resistance heat generated is insufficient to provide the phase transformation energy of metal liquefaction. The heat reaches equilibrium, and the dynamic resistance gradually becomes stable [29]. The current curve shows that the welding equipment can ensure the stability of output current and welding process, and the welding current fluctuates slightly around 9 kA.

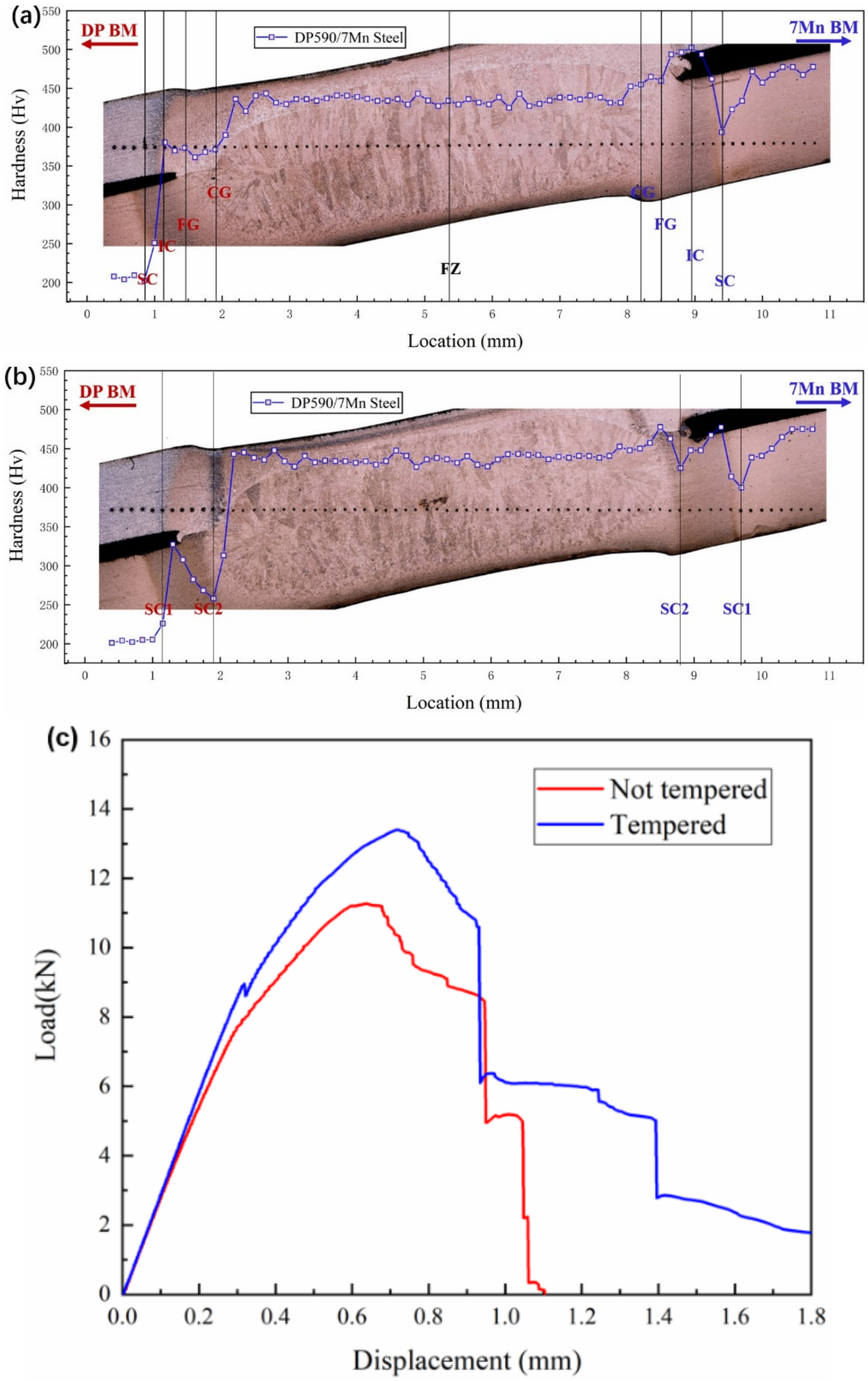

Figure 7. Micro hardness distribution of joint: (**a**) before tempering and (**b**) after tempering. (**c**) Tensile shear test force–displacement curve before and after tempering.

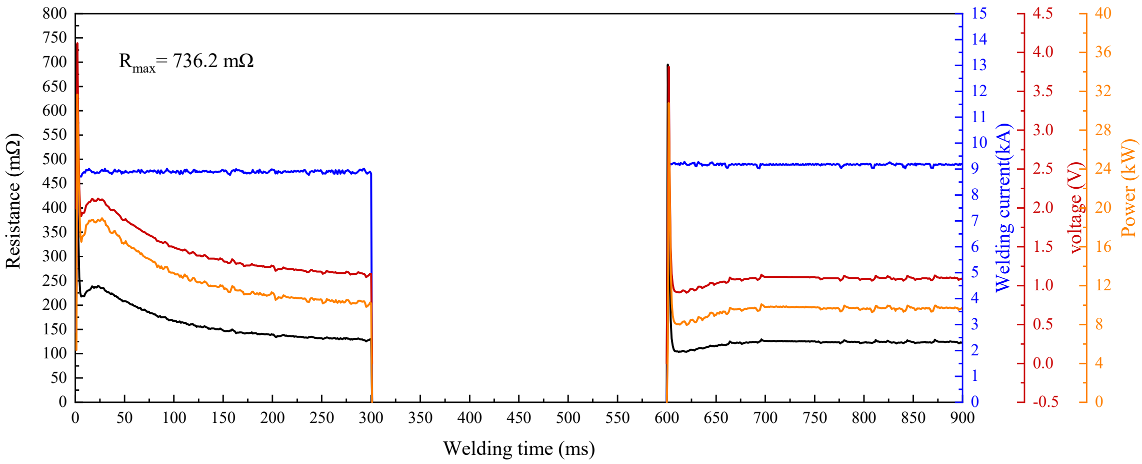

Figure 8. Welding data when tempering current is added.

Figure 9a is the macro-morphology of the 7Mn Steel/DP590 spot-welded joint under the following conditions: single-pulse welding current I = 9 kA, welding time T = 300 ms and electrode pressure F = 4.5 kN. Figure 9b is the macroscopic morphology of the joint, obtained by adding a pulse-tempering current under the optimum process parameters of single pulse, and a tempering current of 7.5 kA. The 7Mn Steel/DP590 dissimilar steel spot-welding joint consists of five different structural zones from left to right: the DP590 base-metal zone (DP590 BM), the DP590-side heat-affected zone (DP590 HAZ), the welding nugget zone (FZ), the 7Mn Steel-side heat-affected zone (7Mn Steel HAZ) and the 7Mn Steel base-metal zone (7Mn Steel BM). The tempered line of the DP590 side is shorter than that of the 7Mn Steel side. This is because DP590 has higher conductivity and thermal conductivity than 7Mn Steel, and the thickness of the DP590 plate is thinner than that of 7Mn Steel. The internal metal involved in the welding process is less and the resistance is lower. According to Joule's law, the heat production of the DP590 side is obviously less than that of the 7Mn Steel side, which leads to the position of the refire line being closer to the nugget. After adding the tempering current, there are two fire lines in the heat-affected zone of the DP590 side.

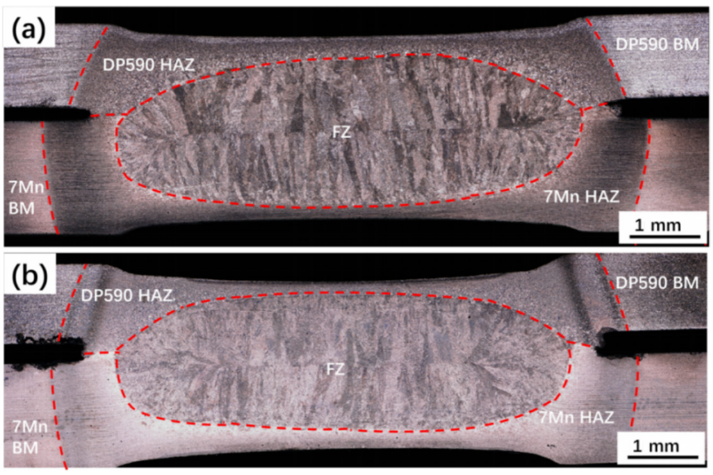

Figure 9. Macro-morphology of joint: (**a**) single pulse; (**b**) with added temper current.

Figure 10 is the microstructure of the nugget zone of medium manganese TRIP steel/DP590. According to the metal solidification theory [30], at the end of the welding stage, the liquid metal began to nucleate at the nugget line and solidified from the edge of the nugget to the center of the nugget. As shown in Figure 10a,d, from the fusion line to the center of the nugget, the crystal forms are planar crystal, cellular crystal, dendritic crystal and columnar crystal. The temperature gradient near the nugget line is very large and the cooling rate is slow. The crystal grows in the form of plane crystal. With the nucleation of liquid metal to the nugget center, the cooling rate increases and the temperature gradient decreases, and the composition under cooling increases gradually. The grain preferentially grows to the nugget center to form columnar crystals, and the growth direction is perpendicular to the crystallization isothermal plane. As shown at point 2 in Figure 10a, on both sides of the nugget zone, the radian of the isothermal surface of the crystallization is large, and the dendrites grow, to a certain extent, in contact with each other, forming columnar crystals with unequal lengths (as shown in Figure 10b, near the center of nugget, the growth direction of the columnar crystal is consistent with the direction of the electrode force) and are finally intertwined at the center line of the nugget. This is because under the action of water cooling the liquid in the electrode, the direction of the electrode force has the fastest heat dissipation and the maximum temperature gradient, and the columnar crystal grows preferentially in the direction of the best heat dissipation. The cooling rate of the welding spot is much faster than the critical speed of the martensitic transformation, and the liquid metal is melted and rapidly solidified. Therefore, the coarse lath martensite structure with a small amount of retained austenite is formed, as shown in Figure 10c.

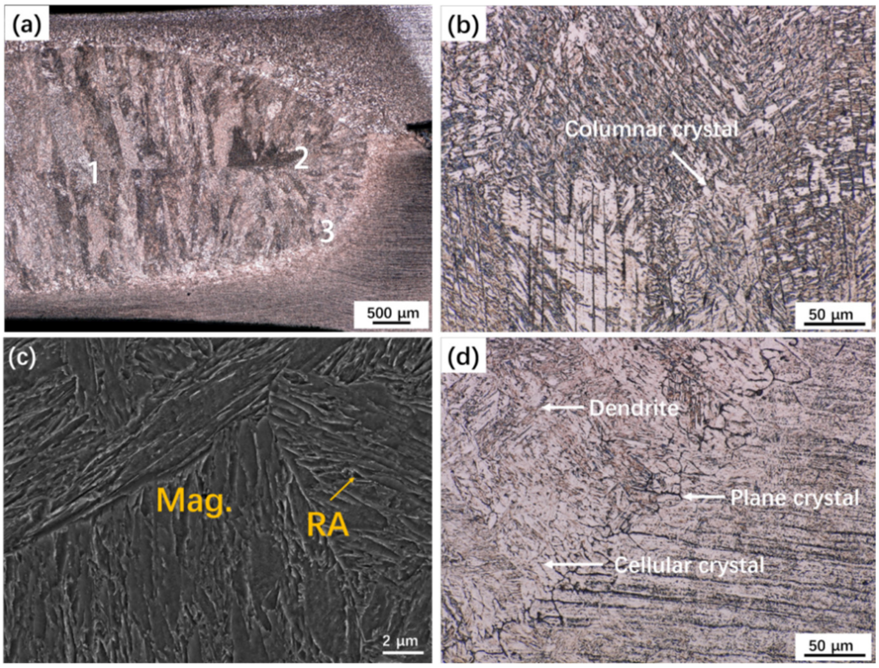

Figure 10. Microstructure of FZ: (**a**) macro-FZ; (**b**) point 1; (**c**) SEM of point 1; (**d**) point 3.

Figure 11 is the microstructure of the DP590-side heat-affected zone, and Figure 11a is the macro-HAZ. According to the distance from the fusion line, the DP590-side heat-affected zone can be divided into four regions: the coarse-grain heat-affected zone (CGHAZ), the fine-grain heat-affected zone (FGHAZ), the partial phase transformation zone (ICHAZ) and the tempering zone (SCHAZ); in the figure, these are 1, 2, 3, and 4. The large amount of grain length in the heat-affected zone is determined by the peak temperature of the position and the time when heating exceeds the austenitizing temperature (AC1). In the CGHAZ next to the FZ, the high cooling rate and large austenite grain size, together with the formation of carbon-rich austenite, promote the formation of coarse block martensite. As shown in Figure 11b, the maximum temperature reached in the FGHAZ is lower than that in the CGHAZ, the time when the temperature exceeds AC1 is shorter, and the size of the martensite generated is smaller, as shown in Figure 11c. When the peak temperature is between AC1 and AC3, the microstructure of the base metal transforms into ferrite and austenite during heating, and the microstructure of the ICHAZ transforms into ferrite and martensite after cooling, as shown in Figure 11d. When the peak temperature is lower than AC1, the island-tempered martensite is formed, which leads to the softening and hardness reduction of the SCHAZ, and the tempering leads to the formation of fine quasi-spherical and lamellar interbedded cementites, expressed by a red arrow in 11e.

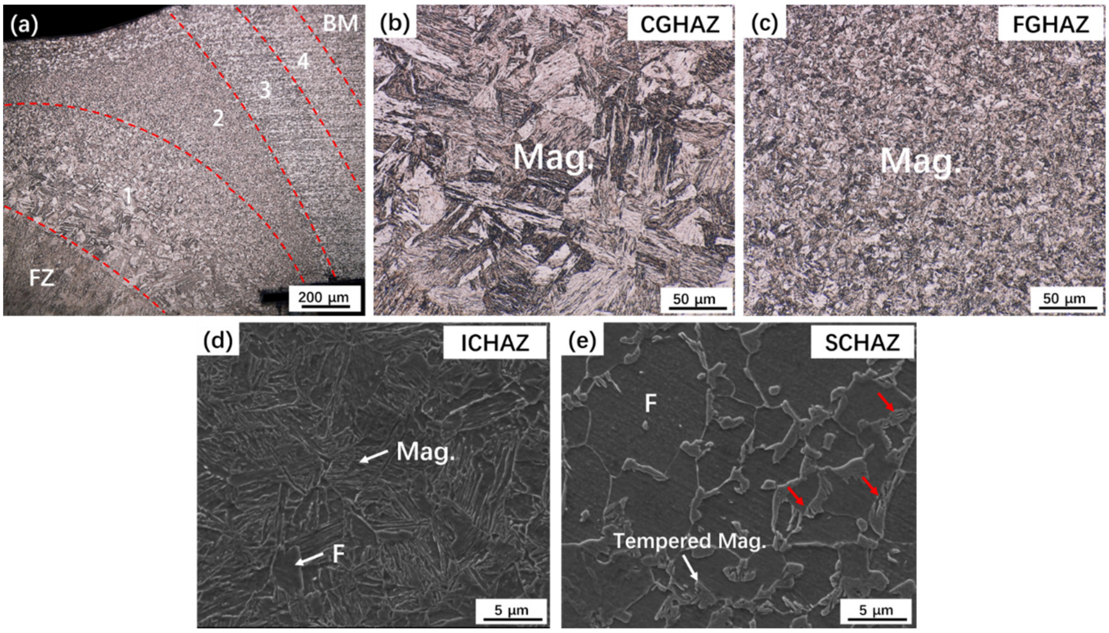

Figure 11. Microstructure of HAZ on DP590 side: (**a**) Macro-HAZ; (**b**) CGHAZ; (**c**) FGHAZ; (**d**) ICHAZ; (**e**) SCHAZ.

Figure 12 is the microstructure of the 7Mn Steel-side heat-affected zone, and Figure 12a is the macro-HAZ. According to the distance from the fusion line, the DP590-side heat-affected zone can be divided into four regions: the coarse-grain heat-affected zone (CGHAZ), the fine-grain heat-affected zone (FGHAZ), the partial phase transformation zone (ICHAZ) and the tempering zone (SCHAZ); in the figure, these are 1, 2, 3, and 4. As shown in Figure 12b, the original austenite grain boundary can be observed in the CGHAZ, and the microstructure is fully transformed martensite. A small amount of spherical residual austenite can be seen on the martensite matrix. As shown in Figure 12c,d, the newly generated austenite transformation island-tempered martensite in the FGHAZ and ICHAZ during the heating process generates the dual-phase structure of the ultrafine-grained ferrite matrix and island-tempered martensite, and the tempered martensite content in the ICHAZ is higher than that in the FGHAZ. As shown in Figure 12e, the SCHAZ region is a duplex microstructure of retained austenite grain and ferrite with ultrafine grains.

Figure 13 shows a cross section of the single-pulse and tempering currents. The welding current is 9 kA, the welding time is 300 ms, the cooling time is 1500 ms and the tempering current is 9.5 kA. It can be seen, in combination with Figure 7, that before adding the tempering current, the softening zone of the heat-affected zone has fracture failure due to the halo effect. After adding the tempering current, the fracture position still occurs in the heat-affected zone of 7Mn Steel, but the necking occurs in the tempering zone generated by the tempering current in the heat-affected zone of the DP590 side. Compared with the fracture section under a single pulse, the hardness of the joint after tempering is greatly reduced, which proves that the halo effect is more obvious, and the softening zone is the cause of joint failure. The study of Figueredo [31] confirmed the existence of a halo, and the overall hardness of the softening zone was reduced by 10%, but the difference is that the hardness change in the heat-affected zone of the 7Mn Steel side after tempering was not obvious. The halo effect was more obvious in the heat-affected zone on the DP590 side. It was found that the halo effect was homogenized, resulting in the failure path being displayed in the surrounding heat-affected zone.

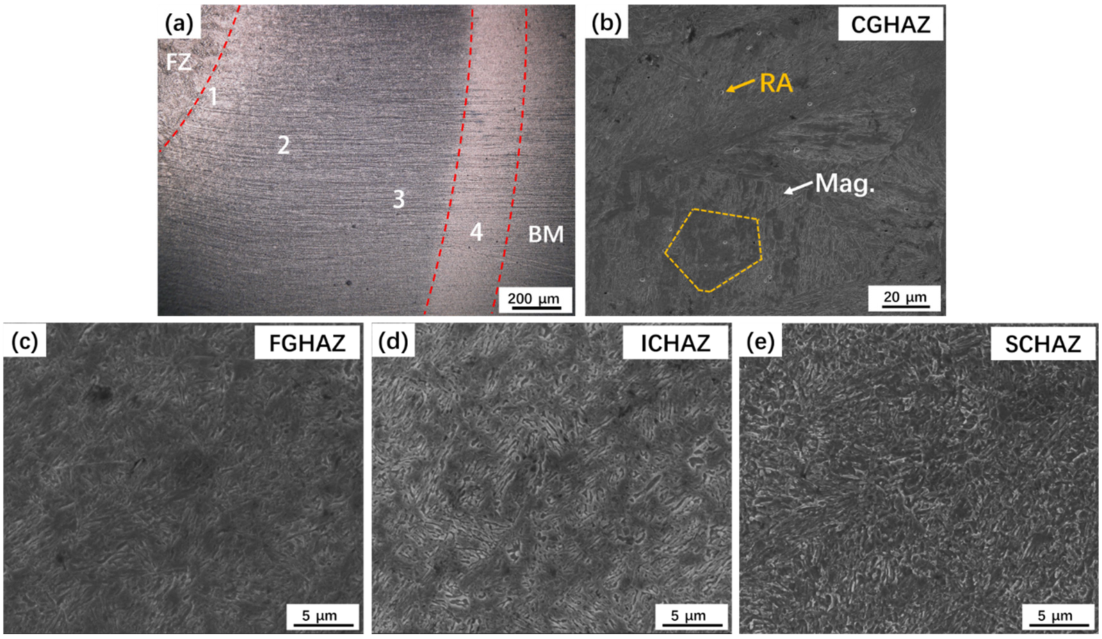

Figure 12. Microstructure of HAZ on 7Mn Steel side: (**a**) Macro-HAZ; (**b**) CGHAZ; (**c**) FGHAZ; (**d**) ICHAZ; (**e**) SCHAZ.

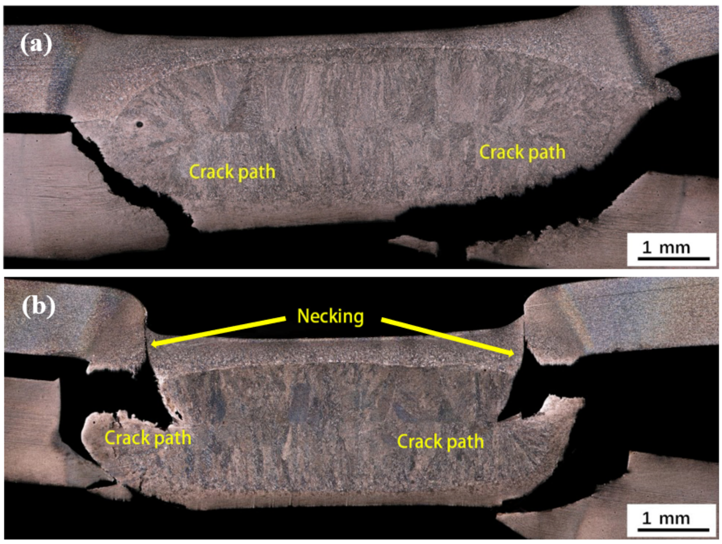

Figure 13. Weld cross-section of welding spot: (**a**) single pulse; (**b**) with added temper current.

4. Conclusions

1. Through the method of control variables, the optimal welding parameters under a single pulse were determined as follows: welding current: 9 kA, welding time: 300 ms and electrode pressure: 4.5 kN. The optimal added tempering process parameters were as follows: tempering current: 7.5 kA, and cooling time: 1500 ms.
2. The nugget diameter and thickness reduction increase with the increase in welding current and welding time. When expulsion occurs, the thickness reduction increases continuously but the nugget diameter decreases. The nugget diameter first increases, and then, decreases with the increase in electrode pressure.

3. The tempered line of the DP590 side is shorter than that of 7Mn Steel side. The microstructure of the tempering zone is composed of island martensite tempering and ferrite, and fine quasi-spherical and lamellar interlayer cementite is formed.
4. There is a strong halo effect in the single-pulse weld, which acts as a failure path. The second pulse of tempering makes the microstructure uniform, resulting in different failure paths and weld strengthening.
5. The failure mode of the welding spot under the single-pulse optimal process is PF-TT failure. After adding the tempering current, the fracture mode does not change, and is still PF-TT failure. The fracture position is still in the heat-affected zone of 7Mn Steel, but the tensile shear force increases from 11.44 kN to 13.4 kN, increasing by 17.13%.

Author Contributions: Literature search, F.W., Y.Z. (Yunming Zhu), Y.T., H.L., Y.Z. (Yongqiang Zhou) and Z.Z., study design, Z.Z., figures, F.W. and Y.Z. (Yunming Zhu), Y.T., H.L. and Y.Z. (Yongqiang Zhou), data collection, F.W. and data analysis, F.W. and data interpretation, F.W. and Y.Z. (Yunming Zhu), Y.T., H.L., Y.Z. (Yongqiang Zhou) and Z.Z., writing—review and editing, F.W., writing—original draft preparation, F.W., Final approval of the version, F.W., Y.Z. (Yunming Zhu), Y.T., H.L., Y.Z. (Yongqiang Zhou) and Z.Z. project administration, Z.Z. All authors have read and agreed to the published version of the manuscript.

Funding: This project was funded by the National Natural Science Foundation of China (51861024), the Jiangxi Provincial Technology Innovation Guidance Program (Science and Technology Cooperation Special Project) (20212BDH81014) and the High-Value Patent Cultivation Project of Nanchang University in 2021.

Institutional Review Board Statement: Not applicable.

Informed Consent Statement: Not applicable.

Data Availability Statement: Not applicable.

Conflicts of Interest: The authors declare no conflict of interest.

References

1. Tisza, M.; Czinege, I. Comparative study of the application of steels and aluminium in lightweight production of automotive parts. *Int. J. Lightweight Mater. Manuf.* **2018**, *1*, 229–238. [CrossRef]
2. Ozsarac, U. Investigation of Mechanical Properties of Galvanized Automotive Sheets Joined by Resistance Spot Welding. *J. Mater. Eng. Perform.* **2012**, *21*, 748–755. [CrossRef]
3. Basak, S.; Das, H.; Pal, T.K.; Shome, M. Characterization of intermetallics in aluminum to zinc coated interstitial free steel joining by pulsed MIG brazing for automotive application. *Mater. Charact.* **2016**, *112*, 229–237. [CrossRef]
4. Han, C. Research on the Development and Application of Lightweight Automotive Materials. *J. Phys. Conf. Ser. IOP Publ.* **2020**, *1676*, 012085. [CrossRef]
5. Tekkaya, A.E.; Min, J. Special Issue on Automotive Lightweight. *Automot. Innov.* **2020**, *3*, 193–194. [CrossRef] [PubMed]
6. Buchely, M.F.; Field, D.M.; Van Aken, D.C. Analysis of Hot- and Cold-Rolled Loads in Medium-Mn TRIP Steels. *Metall. Mater. Trans. B* **2019**, *50*, 1180–1192. [CrossRef]
7. Field, D.M.; Qing, J.; Van Aken, D.C. Chemistry and Properties of Medium-Mn Two-Stage TRIP Steels. *Metall. Mater. Trans. A* **2018**, *4*, 4615–4632. [CrossRef]
8. Li, Z.C.; Zhang, X.T.; Mou, Y.J.; Misra, R.D.; He, L.F.; Li, H.P. The impact of intercritical annealing in conjunction with warm deformation process on microstructure, mechanical properties and TRIP effect in medium-Mn TRIP steels. *Mater. Sci. Eng. A* **2019**, *746*, 363–371. [CrossRef]
9. Suh, D.; Kim, S. Medium Mn transformation-induced plasticity steels: Recent progress and challenges. *Scr. Mater.* **2017**, *126*, 63–67. [CrossRef]
10. Saeidi, N.; Jafari, M.; Kim, J.G.; Ashrafizadeh, F.; Kim, H.S. Development of an Advanced Ultrahigh Strength TRIP Steel and Evaluation of Its Unique Strain Hardening Behavior. *Met. Mater. Int.* **2020**, *26*, 168–178. [CrossRef]
11. Park, G.; Uhm, S.; Lee, C. Effects of in-situ post-weld heat treatment on the microstructure and mechanical properties of the coarse-grained heat-affected zone in a resistance spot weld in medium Mn TRIP steel. *Mater. Sci. Eng. A* **2020**, *788*, 139477. [CrossRef]
12. Verma, J.; Taiwade, R.V. Effect of welding processes and conditions on the microstructure, mechanical properties and corrosion resistance of duplex stainless steel weldments—A review. *J. Manuf. Process.* **2017**, *25*, 134–152. [CrossRef]
13. Tunçel, O.; Aydin, H.; Çetin, Ş. Microstructure and mechanical properties of similar and dissimilar laser welds of dp600 and dp1000 steel sheets used in the automotive industry. *Turk. J. Eng.* **2021**, *5*, 8–14. [CrossRef]

14. Messler, J.R.W.; Jou, M. Review of control systems for resistance spot welding: Past and current practices and emerging trends. *Sci. Technol. Weld. Join.* **2014**, *1*, 1–9. [CrossRef]
15. Martín, O.; Tiedra, P.D.; San-Juan, M. Combined effect of resistance spot welding and precipitation hardening on tensile shear load bearing capacity of A286 superalloy. *Mater. Sci. Eng. A* **2017**, *688*, 309–314. [CrossRef]
16. Akkaş, N. Welding Time Effect on Tensile-Shear Loading in Resistance Spot Welding of SPA-H Weathering Steel Sheets Used in Railway Vehicles. *Acta Phys. Pol.* **2017**, *131*, 52–54. [CrossRef]
17. Ji, X.; Han, X.; Zhou, M.; Liu, J. Effect of Heat treatment on the slurry erosion resistance of high strength steel DP980. *Int. J. Mater. Res.* **2014**, *105*, 487–492. [CrossRef]
18. Jia, Q.; Liu, L.; Guo, W.; Peng, Y.; Zou, G.; Tian, Z.; Zhou, Y.N. Microstructure and Tensile-Shear Properties of Resistance Spot-Welded Medium Mn Steel. *Met. Open Access Metall. J.* **2018**, *8*, 48. [CrossRef]
19. Park, G.; Kim, K.; Uhm, S.; Lee, C. A comparison of cross-tension properties and fracture behavior between similar and dissimilar resistance spot-weldments in medium-Mn TRIP steel. *Mater. Sci. Eng. A* **2019**, *752*, 206–216. [CrossRef]
20. Park, G.; Kim, K.; Uhm, S.; Lee, C. Remarkable improvement in resistance spot weldability of medium-Mn TRIP steel by paint-baking heat treatment. *Mater. Sci. Eng.* **2019**, *766*, 138401. [CrossRef]
21. Li, S.; Yang, S.; Lu, Q.; Luo, H.; Tao, W. A Novel Shim-Assisted Resistance Spot Welding Process to Improve Weldability of Medium-Mn Transformation-Induced Plasticity Steel. *Metall. Mater. Trans. B* **2018**, *50*, 1–9. [CrossRef]
22. Sun, B.; Fazeli, F.; Scott, C.; Brodusch, N.; Gauvin, R.; Yue, S. The influence of silicon additions on the deformation behavior of austenite-ferrite duplex medium manganese steels. *Acta Mater.* **2018**, *148*, 249–262. [CrossRef]
23. Liu, C.; Peng, Q.; Xue, Z.; Wang, S.; Yang, C. Microstructure and Mechanical Properties of Hot- Rolled and Cold-Rolled Medium-Mn TRIP Steels. *Materials* **2018**, *11*, 2242. [CrossRef]
24. Lun, N.; Saha, D.C.; Macwan, A.; Pan, H.; Wang, L.; Goodwin, F.; Zhou, Y. Microstructure and mechanical properties of fibre laser welded medium manganese TRIP steel. *Mater. Des.* **2017**, *131*, 450–459. [CrossRef]
25. Liangyu, C.; Zhanjiang, W. Carbon equivalent formula of steel and its application in welding. *Mater. Dev. Appl.* **1999**, *14*, 39–45.
26. Pouranvari, M.; Abedi, A.; Marashi, P.; Goodarzi, M. Effect of expulsion on peak load and energy absorption of low carbon steel resistance spot welds. *Sci. Technol. Weld. Join.* **2008**, *13*, 39–43. [CrossRef]
27. Feng, Q.; Zhu, Y.; Zhao, H. Research on Resistance Spot Welding of DP980 Dual Phase Steel. *Adv. Mater. Res.* **2013**, *860–863*, 780–783. [CrossRef]
28. Sherepenko, O.; Jüttner, S. Transient softening at the fusion boundary in resistance spot welded ultra-high strengths steel 22MnB5 and its impact on fracture processes. *Weld World* **2019**, *63*, 151–159. [CrossRef]
29. Cho, Y.; Rhee, S. New technology for measuring dynamic resistance and estimating strength in resistance spot welding. *Meas. Sci. Technol.* **2000**, *11*, 1173. [CrossRef]
30. Fu, H.Z.; Liu, L. *Progress of Directional Solidification in Processing of Advanced Materials: Materials Science Forum*; Trans Tech Publications: Zurich, Switzerland, 2005.
31. Figueredo, B.; Ramachandran, D.C.; Macwan, A.; Biro, E. Failure behavior and mechanical properties in the resistance spot welding of quenched and partitioned (Q&P) steels. *Weld. World* **2021**, *65*, 2359–2369. [CrossRef]